


## Article

# Thermal Behavior of Pyromorphite ( $\text{Pb}_{10}(\text{PO}_4)_6\text{Cl}_2$ ): In Situ High Temperature Powder X-ray Diffraction Study

Tingting Gu <sup>1,\*</sup> , Shan Qin <sup>2</sup> and Xiang Wu <sup>3</sup><sup>1</sup> Gemological Institute of America, 50 W, 47th Street, New York, NY 10036, USA<sup>2</sup> Key Laboratory of Orogenic Belts and Crustal Evolution, Ministry of Education, School of Earth and Space Sciences, Peking University, Beijing 100871, China; sqin@pku.edu.cn<sup>3</sup> State Key Laboratory of Geological Processes and Mineral Resources, China University of Geosciences, Wuhan 430074, China; wuxiang@cug.edu.cn

\* Correspondence: gtt.pku@gmail.com

Received: 14 October 2020; Accepted: 16 November 2020; Published: 24 November 2020



**Abstract:** Pyromorphite is one of the important end member lead apatites that has potential applications in environment remediation. The thermal behavior of natural pyromorphite,  $\text{Pb}_{10}(\text{PO}_4)_6\text{Cl}_2$ , has been investigated up to 1373 K at room-pressure using a powder X-ray diffraction device equipped with a heating system. Pyromorphite experiences melting and decomposing at 1373 K into lead phosphate ( $\text{Pb}_3(\text{PO}_4)_2$ ), and lead dioxide ( $\text{PbO}_2$ ) with reaction with air. The fit of the temperature–volume data yields a linear volume expansion coefficient  $\alpha_V = 4.5 (\pm 0.02) \times 10^{-5} \text{ K}^{-1}$ . The linear expansion coefficients for lattice parameters present the anisotropic thermal expansibility, i.e.,  $\alpha_a = (\pm 0.06) \times 10^{-5} \text{ K}^{-1}$  and  $\alpha_c = 2.2 (\pm 0.06) \times 10^{-5} \text{ K}^{-1}$ . We looked into the crystal chemistry and proposed an expression to quantitatively evaluate the structural evolution of pyromorphite upon high temperature by calculating the twist angle of the  $\text{Pb}(1)\text{O}_6$  metaprism, which decreases at elevated temperatures. A distinct drop of the twist angle was observed at ~1100–1200 K, which might be a sign for the phase transition to a low symmetric subgroup. The variation of the twist angle is more sensitive than that of the unit cell; therefore, it can be applied to monitor the structural and phase changes of apatite group materials in general.

**Keywords:** pyromorphite; apatite; high-temperature; in situ X-ray diffraction; thermal expansion

## 1. Introduction

Apatite has a general formula of  $\text{A}_5(\text{BO}_4)_3\text{X}$ , where A is usually a divalent cation such as  $\text{Ca}^{2+}$ ,  $\text{Sr}^{2+}$ ,  $\text{Ba}^{2+}$ ,  $\text{Pb}^{2+}$ , and  $\text{Cd}^{2+}$ ; B is usually the anions with tetrahedral coordination, such as  $\text{PO}_4^{3-}$ ,  $\text{AsO}_4^{3-}$ ,  $\text{VO}_4^{3-}$ ,  $\text{SO}_4^{2-}$ , or  $\text{SiO}_4^{2-}$ ; and X is a monovalent electronegative anion such as  $\text{OH}^-$  or halide [1]. The structural prototype for the apatite family has  $P6_3/mcm$  (193) symmetry [2], which can be deviated into several subgroups such as  $Cmcm$  (63),  $P6_3/m$  (176), and  $P6_3cm$  (185) [3]. In a typical apatite structure, there are two crystallographically distinct A sites. The  $\text{A}(1)\text{O}_6$  metaprisms share edges with  $\text{BO}_4$  tetrahedra and build up zeolite-like channels alongside the [001] direction. Meanwhile, the  $\text{A}(2)$  atoms form two [001] triangles rotated with an angle ( $60^\circ$  for an ideal apatite structure) and connect between the  $\text{BO}_4$  tetrahedra outside the edges of the channel. The unique arrangement of the apatite channel structure allows it to accommodate multivalent large cations. Therefore, in Earth science, apatite is the most abundant rock-forming phosphate-group and the dominant reservoirs for both rare Earth elements (REEs) and volatile elements (F, Cl, OH) [4]. They often occurred as the minor phase in igneous and metamorphic rocks on Earth, which is considered as the primary carrier of the bulk  $\text{P}_2\text{O}_5$  in continental and oceanic crust ~0.19 wt.% [5]. Apatite is also a common

mineral in terrestrial bodies, where it occurs as the late-stage crystallization products of magmas, which can be found ubiquitously as a magmatic mineral in SNC groups of Martian meteorites. Moreover, lunar apatite has been considered as an important host for water in the moon's interior [6]. Therefore, the structural behavior of apatite under high temperature is important for us to understand the fate of apatite during the magma process as well as in the planetary deep regions.

Moreover, apatite has found applications in catalysis; bone replacement; as well as immobilizing hazardous elements such as Pb, As, Cr, Cd, and Pu in contaminated water, soil, and hazardous industrial wastes [7–9]. Lead apatite, such as the end member minerals pyromorphite  $\text{Pb}_{10}(\text{PO}_4)_6\text{Cl}_2$ , mimetite  $\text{Pb}_{10}(\text{AsO}_4)_6\text{Cl}_2$ , and vanadinite  $\text{Pb}_5(\text{VO}_4)_3\text{Cl}$ , can be the final products of environmental remediation [7,8]; therefore, their thermal stabilities and chemical properties are important for utilizing apatite as the agent in hazardous waste treatment. So far, the thermal properties of  $\text{Ca}_{10}(\text{PO}_4)_6(\text{F}, \text{OH}, \text{Cl})_2$  solid solutions have been studied by X-ray diffraction under high temperature, and their thermal expansion coefficients have been obtained [10,11]. Pyromorphite  $\text{Pb}_{10}(\text{PO}_4)_6\text{Cl}_2$  is one of the important end member lead phosphates; the substitution of Pb in the lattice contributes to the deviation from the general  $P6_3/mcm$  symmetry of apatite to  $P6_3/m$ , with  $Z = 2$ , which will affect the thermal properties of the mineral under high temperature. However, so far, the study of the thermal property of pyromorphite is relatively limited. In the previous studies, the thermal properties of pyromorphite have been investigated by differential thermal analysis (DTA) [12,13] and X-ray diffraction [12,13]. The DTA study revealed a phase transition of pyromorphite at 1081 K [12,13], while in an early study, no endothermic peak of pyromorphite was observed before melting [14], and it is unclear if the endothermic peak observed in DTA was related to any other forms of crystalline transition. In this paper, we would like to look into the crystal chemistry and lattice dynamics of pyromorphite under high temperature to investigate the phase transition and structural evolution of pyromorphite in situ under high temperature from ambient condition to the melting temperature. By introducing the twist angle of Pb2 triangles on [0001], we would like to explore a way to efficiently monitor the structural evolution of pyromorphite under verified environments, which can be applied to similar apatite group materials.

## 2. Materials and Methods

The natural pyromorphite crystal with yellow-green and perfect hexagonal prism form was collected in Daoping, Guangxi province as the study sample. The well crystalized sample was grounded into powder and the in situ high temperature powder X-ray diffraction (XRD) experiment was carried out using an X' Pert PRO X-ray diffractometer equipped with a heating platform. Graphite filtered Cu  $K_\alpha$  radiation at a voltage of 40 kV and a current of 45 mA was applied. The scattered radiation was detected in the angular range of 10–80° ( $2\theta$ ), with scan step time 1 s, a step of 0.0170° ( $2\theta$ ), and 1 s time interval.

The diffraction data were recorded at an elevated temperature from 298 K (room temperature, RT) to 1373 K. At each temperature interval, the sample was heated to the next measured temperature at a rate of 5 K/min and kept at that temperature with a two-minute stop. At the highest temperature (1373 K), the sample was cooled down to RT at a rate of about −20 K/min. Finally, the recovered sample from a high temperature was examined by XRD. The lattice parameters of pyromorphite were calculated by the Reitveld refinement method implemented in GSAS software [15]. We followed the strategy of Rietveld refinement instructed in the literature [15] and refined the positions of the heavier atoms first and then those of the lighter atoms at each temperature.

## 3. Results and Discussion

### 3.1. XRD Patterns

Figure 1 represents the selected XRD patterns recorded from RT to 1273 K. All the diffraction peaks for each heating pattern can be indexed to pyromorphite. The unit cell parameters obtained at ambient condition are  $a = 9.9896(1) \text{ \AA}$ ,  $c = 7.3457(2) \text{ \AA}$ , and  $V = 634.83(1) \text{ \AA}^3$ , which are within 0.2%

discrepancy compared with the data in the literature for pure pyromorphite (i.e.,  $a = 9.976 \text{ \AA}$ ,  $c = 7.351 \text{ \AA}$ , and  $V = 633.6 \text{ \AA}^3$  [16]), and confirm that the sample is in a single pyromorphite phase, and the impure elements should be at a minimum. As temperature increases, the diffraction peaks shift to lower angles accompanied by the decreasing of the relative intensity under elevated temperatures. For example, the position of the 113 reflection moves from  $41.033^\circ$  to  $40.268^\circ$  ( $2\theta$ ) with temperature increasing from 298 K to 1273 K. We observed that the fitting accuracy decreases after the temperature reaches  $\sim 1100 \text{ K}$ . Besides, a discontinuous change of cell parameters at around  $1100\text{--}1200 \text{ K}$  can be detected (Figure 2), which might be related to a phase transition. In previous studies, a small endothermic peak was observed at  $\sim 1081 \text{ K}$  and the new phase was identified by XRD as a monoclinic structure (space group  $P112_1/b$ ) [12]. In contrast, no phase transition was observed by DTA for pyromorphite from 373 to 1273 K [14], and no phase transitions were observed by DTA for Ca and Pb apatite solid solutions ( $\text{Ca}_{10x}\text{Pb}_{10-10x}(\text{PO}_4)_6\text{Cl}_2$ ) before melting [13]. Therefore, the phase transition from  $P6_3/m$  to the monoclinic subgroup could be very subtle in powder X-ray patterns, and with our experimental resolution, all the XRD peaks can still be indexed with the  $P6_3/m$  structure before melting. At the maximum temperature (1373 K) in this study, the XRD data show a diagnostics pattern of an amorphous phase (Figure 2a), indicating that pyromorphite is melting. The melting temperature is consistent with the endothermic peak observed at 1415 K by differential thermal analysis [12].

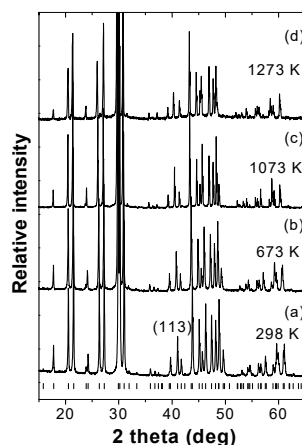


**Figure 1.** Selected X-ray diffraction (XRD) patterns of pyromorphite at varied temperatures. (a) XRD pattern collected at room temperature (298 K). The bottom ticks are the positions of the reflections. 113 reflection is highlighted to monitor the shift of the pattern at high temperature. (b–d) XRD patterns collected at 673, 1073 and 1273 K respectively, which show a shift to the lower angle. The background of the XRD pattern is rising at 1273 K.

We also examined the recovered product from the melted materials at ambient condition by XRD (Figure 2b), and found that the melt product can not completely re-crystallize into pyromorphite even at a cooling rate of about  $-20 \text{ K/min}$ . The XRD pattern of the final products can be indexed and assigned to three phases, i.e., the remained pyromorphite and lead phosphate ( $\text{Pb}_3(\text{PO}_4)_2$ ), as well as two peaks detected at  $\sim 27.3^\circ$  and  $28.9^\circ$  that match with the (111) and (020) peaks of lead dioxide ( $\text{PbO}_2$ ). Therefore, the XRD results indicate that pyromorphite becomes thermally instable at 1373 K and starts to decompose into lead phosphate at this temperature. The lead dioxide can be a side product of the oxidized  $\text{PbCl}_2$  decomposed from pyromorphite during heating in an open environment. With our experimental setup, the released  $\text{Cl}_2$  could prohibit a complete oxidation of the final products and yield lead dioxide together with lead phosphate, i.e.,  $(\text{Pb}_{10}(\text{PO}_4)_6\text{Cl}_2) + \text{O}_2 \rightarrow 3\text{Pb}_3(\text{PO}_4)_2 + \text{PbO}_2 + \text{Cl}_2$ .  $\text{PbO}_2$  has been considered as the highly insoluble lead dioxide solid, which is stable with water of persistently high oxidation-reduction potential, usually achieved by maintaining adequate levels of free chlorine in waters [17]. Therefore, pyromorphite can potentially be an ideal agent at the relatively high temperature for water treatment or soil remediation.

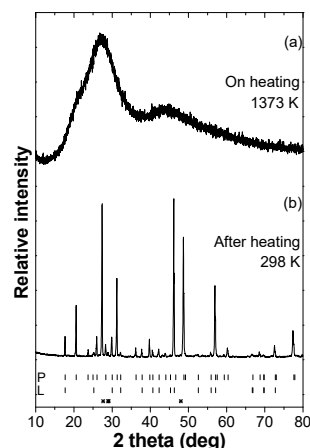


**Figure 2.** The XRD pattern of the melted materials of pyromorphite. Upper (a), on heating at  $T = 1373$  K; lower (b), after heating at  $T = 298$ . Key to peaks label abbreviations:  $p$  = pyromorphite ( $\text{Pb}_{10}(\text{PO}_4)_6\text{Cl}_2$ );  $L$  = lead phosphate ( $\text{Pb}_3(\text{PO}_4)_2$ ); \* is indexed as the peaks from lead dioxide ( $\text{PbO}_2$ ).

### 3.2. Unit-Cell Parameters and Thermal Expansibility

The lattice parameters of pyromorphite under high temperature are listed in Table 1. The fitting goodness parameter (wRp, no effect of the background) is acceptable under a low temperature ( $\sim 10\%$ , which is typical for laboratory X-ray data [15]); however, it becomes larger with increasing temperature because the signal ratio of XRD data at a higher temperature is worse than those at a lower temperature (see Figure 1a–d), indicating that the structure deviates more at a higher temperature. Above 1200 K, the background of the XRD pattern is rising (Figure 1d), implying an increasing amount of amorphous material that could be generated during partial melting.

**Table 1.** Lattice parameters and twist angles of pyromorphite at different temperatures.

T/K	$a/\text{\AA}$	$c/\text{\AA}$	$V/\text{\AA}^3$	$a/c$	$\phi/^\circ$	wRp/%
298	9.9896 (1)	7.3457 (2)	634.83 (1)	1.356	21.8 (2)	12.57
373	9.9973 (2)	7.3540 (2)	636.53 (2)	1.359	21.3 (2)	10.37
423	10.0036 (1)	7.3610 (1)	637.94 (1)	1.359	20.7 (2)	10.53
473	10.0050 (2)	7.3646 (2)	638.44 (2)	1.359	21.2 (2)	13.51
673	10.0365 (2)	7.3978 (2)	645.36 (2)	1.357	20.4 (2)	12.57
873	10.0606 (2)	7.4262 (3)	650.94 (3)	1.355	20.8 (3)	24.95
1073	10.0846 (3)	7.4612 (4)	657.14 (4)	1.352	20.0 (3)	30.50
1123	10.0886 (3)	7.4715 (3)	658.57 (4)	1.350	19.5 (4)	29.72
1173	10.0920 (3)	7.4793 (3)	659.68 (3)	1.349	20.1 (3)	28.85
1223	10.0878 (4)	7.4977 (4)	660.78 (5)	1.345	17.6 (3)	25.02
1273	10.0830 (3)	7.5062 (3)	660.90 (4)	1.343	10.4 (5)	19.93

Note: The numbers in parentheses represent one standard deviation in the right-most digit. wRp is the goodness parameter for the Reitveld refinement using GSAS.

Based on the lattice cell parameters under different temperatures (Table 1), we fit them as a function of temperature with a linear model. The temperature dependence of the unit-cell parameters, normalized to the values at 298 K, is illustrated in Figure 3, where the data of chlorapatite are also plotted for comparison [12,18]. The thermal expansion coefficient of volume yielded by the linear fitting,  $\alpha_V$ , is  $4.5 (\pm 0.02) \times 10^{-5} \text{ K}^{-1}$ , close to the  $\alpha_V$  values of calcium apatite members. For example, the  $\alpha_V$  of hydroxylapatite, fluorapatite, and chlorapatite are  $4.24 \times 10^{-5} \text{ K}^{-1}$  [10],  $4.15 \times 10^{-5} \text{ K}^{-1}$ , and  $4.19 \times 10^{-5} \text{ K}^{-1}$  [11] during 293–875 K and 293–1173 K, respectively. The results indicate that, although the effective ionic radius of  $\text{Pb}^{2+}$  (1.33 Å) is bigger than that of  $\text{Ca}^{2+}$  (1.14 Å) [19], the thermal expansion coefficient ( $\alpha_V$ ) is not very sensitive to ionic radius. However, the expansion coefficients show a distinct difference along different crystallographic axes, i.e., the  $\alpha_c$ ,  $2.2 (\pm 0.06) \times 10^{-5} \text{ K}^{-1}$

is nearly twice as large as the  $\alpha_a$ ,  $1.1 (\pm 0.06) \times 10^{-5} \text{ K}^{-1}$ , indicating a notable anisotropy of thermal expansibility. However, the thermal anisotropy is not as strong as that of chlorapatite (Figure 3, Table 2). Therefore, the substitution of bigger cation could potentially reduce the thermal anisotropy of the apatite materials. A similar trend can be found for  $\text{Cd}_5(\text{PO}_4)_3\text{Cl}$  and  $\text{Ba}_5(\text{PO}_4)_3\text{Cl}$ , where with a smaller radius of  $\text{Cd}^{2+}$  ( $1.09 \text{ \AA}$ ),  $\text{Cd}_5(\text{PO}_4)_3\text{Cl}$  shows a more obvious thermal anisotropy ( $\alpha_a = 0.17 \times 10^{-5} \text{ K}^{-1}$ ,  $\alpha_c = 2.35 \times 10^{-5} \text{ K}^{-1}$ ) than that of  $\text{Ba}_5(\text{PO}_4)_3\text{Cl}$  ( $r_{\text{Ba}^{2+}} = 1.49 \text{ \AA}$ ), whose  $\alpha_a$  and  $\alpha_c$  are very close to each other (within  $\sim 10\%$ ) [12].

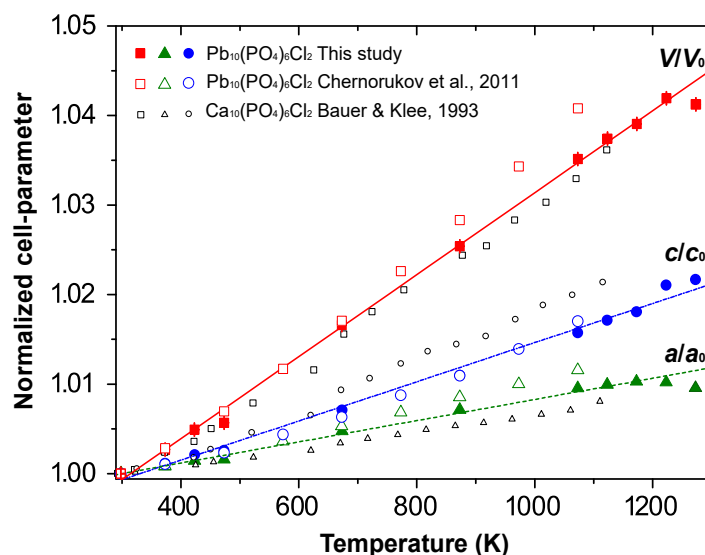


**Figure 3.** Variation of lattice parameters, normalized to the values at 298 K, as a function of temperature. Previous data for pyromorphite [12] and chlorapatite [18] are plotted for comparison.

### 3.3. Thermal Effects on Crystal Structure

Pyromorphite has a  $P6_3/m$  apatite structure. As shown in Figure 4, the crystal structure of pyromorphite can be simply described as  $\text{PO}_4$  tetrahedra linking with  $\text{Pb}(1)\text{O}_6$  metaprisms by sharing corners, and with  $\text{Pb}(2)\text{O}_4\text{Cl}_2$  trigonal prisms by sharing edges. The  $\text{Pb}(1)\text{O}_6$  metaprism can be considered as a twisted trigonal prism, an intermediate form between a trigonal prism and an octahedron. The amount of twisting, referred to the metaprism twist angle ( $\phi$ , the angle  $\text{O}(1)\text{--Pb}(1)\text{--O}(2)$  projected on  $(0001)$ , see Figure 4), can reflect the structural evolution under different conditions.

**Table 2.** Thermal expansion coefficients based on linear fits of pyromorphite compared with other calcium or chlorine bearing apatites.

	$\alpha_V (\times 10^{-5} \text{ K}^{-1})$	$\alpha_a (\times 10^{-5} \text{ K}^{-1})$	$\alpha_c (\times 10^{-5} \text{ K}^{-1})$	Reference
$\text{Pb}_{10}(\text{PO}_4)_6\text{Cl}_2$	$4.5 (\pm 0.02)$	$1.1 (\pm 0.06)$	$2.2 (\pm 0.06)$	This Study
$\text{Ca}_{10}(\text{PO}_4)_6\text{Cl}_2$	4.19	0.96	2.22	[10,11]
$\text{Ca}_{10}(\text{PO}_4)_6\text{F}_2$	4.15	1.38	1.32	[10,11]
$\text{Ca}_{10}(\text{PO}_4)_6(\text{OH})_2$	4.24	—	—	[10,11]
$\text{Cd}_5(\text{PO}_4)_3\text{Cl}$	2.7	0.17	2.35	[12]

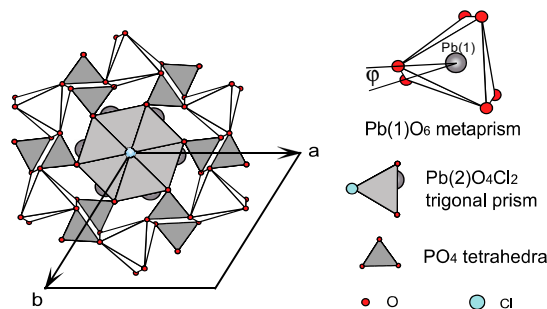


**Figure 4.** The pyromorphite structure projected along [0001], showing the  $\text{PO}_4$  tetrahedra, the  $\text{Pb(2)O}_4\text{Cl}_2$  trigonal prism and the twist angle of  $\text{Pb(1)O}_6$  metaprism.

To have a more in-depth understanding of the structural evolution under high temperature, here, we propose a quantitative expression of the twist angle  $\phi$  adapted from a previous study [2] in terms of the fractional coordinates of Pb(1), O(1), and O(2), which can be used to calculate the twist angle  $\phi$  for pyromorphite as well as other  $P6_3/m$  apatites:

$$\cos \phi = \frac{M^2 + N^2 - L^2}{2\sqrt{M \cdot N}} \quad (1)$$

where  $M = [(x_{\text{Pb1}} - x_{\text{O1}})^2 + (y_{\text{Pb1}} - y_{\text{O1}})^2]^{0.5}$ ,  $N = [(x_{\text{Pb1}} - x_{\text{O2}})^2 + (y_{\text{Pb1}} - y_{\text{O2}})^2]^{0.5}$ , and  $L = [(x_{\text{O2}} - x_{\text{O1}})^2 + (y_{\text{O2}} - y_{\text{O1}})^2]^{0.5}$ .  $x$  and  $y$  represent atom positions;  $M$ ,  $N$ , and  $L$  stand for the lengths of Pb(1)–O(1), Pb(1)–O(2), and O(1)–O(2), respectively, projected on (0001) of the  $\text{Pb(1)O}_6$  metaprism.

The refined atom coordinates were enclosed in the cif format files in Supplementary Materials and the calculated twist angles are listed in Table 1. The temperature dependence of the twist angle  $\phi$  is plotted in Figure 5. We found that the twist angle is very sensitive to the structure evolution under a high temperature. The twist angle decreases from  $21.8^\circ$  to  $\sim 19.5^\circ$  with the temperature increasing from 298 K to 1123 K. Although restricted by the experimental setup, the atom coordinates refined in this study are relatively rough, the decreasing trend of the twist angle can still be detected given that each data point was collected in the same system. We fitted the data linearly and the first-order coefficient of the decreasing of the twist angle is  $-8.4 (\pm 1.7) \times 10^{-5} \text{ K}^{-1}$ , with  $R^2 = 0.88$ , and the absolute value is notably higher than that of thermal coefficients of  $\alpha_a$ ,  $\alpha_c$ , and  $\alpha_V$  (i.e.,  $\sim 1.1\text{--}4.5 \times 10^{-5} \text{ K}^{-1}$ ), indicating that the variation of the twist angle is more sensitive to the change of volume and lattice parameters. Moreover, a distinct drop of the twist angle was observed at  $\sim 1100\text{--}1200 \text{ K}$ , which is consistent with the discontinuity of the cell parameters. The sudden decrease of the twist angle would be a sign that the  $P6_3/m$  structure collapses at this temperature range, which could correspond to the previous observation of the phase transition to  $P112_1/b$  structure at  $\sim 1100 \text{ K}$  [12].

In apatite group materials, the smallest twist angle ( $\phi = 5.2^\circ$ ) was observed in  $\text{Ca}_2\text{Pb}_3(\text{AsO}_4)_3\text{Cl}$ , and the largest twist angle ( $\phi = 26.7^\circ$ ) was found for  $\text{Pb}_5(\text{PO}_4)_3\text{OH}$  [2]. The decrease of the twist angle reflects the increasing average ionic radius under a high temperature. In fact, smaller twist angles are accompanied by the collapse of the structure, which lead to an expansion of the  $\text{Pb(1)O}_6$  metaprism and longer cell edges. The observation under a high temperature is consistent with that of apatite group minerals at ambient conditions with different substitutional atoms, which shows that the twist angle decreases linearly as a function of the increasing average ionic radius of the formula unit [2]. We found that the changing rate of the twist angle is more obvious than the individual lattice length at the same condition; therefore, the phase transition of apatite and its structural development can be effectively monitored by the deviation of the twist angle  $\phi$ .



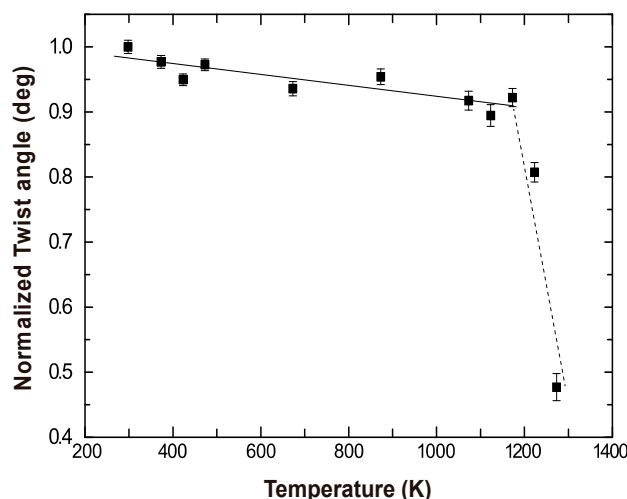


**Figure 5.** The temperature dependence of the twist angle  $\phi$  of pyromorphite, from 298 K to 873 K, normalized to the value at 298 K.

#### 4. Conclusions

With a powder XRD device equipped with a heating system, nature pyromorphite was investigated up to 1373 K at ambient pressure. The powder XRD patterns show that the lattice and volume of pyromorphite increase upon elevated temperature, and a discontinuous change of the lattice parameter was observed around 1100–1200 K. After melting at 1373 K, by interaction with air, pyromorphite decomposes and reacts into lead phosphate ( $\text{Pb}_3(\text{PO}_4)_2$ ) and lead dioxide ( $\text{PbO}_2$ ). The low solubility of the final products can add advantage for pyromorphite to be an agent of environment remediation. The thermal expansion coefficients of pyromorphite ( $4.5 (\pm 0.02) \times 10^{-5} \text{ K}^{-1}$ ) are close to that of calcium apatites. However, the anisotropic thermal expansibility of pyromorphite was observed to be weaker than that of chlorapatite. The different linear expansive coefficients for lattice parameters are  $\phi_c = (\pm 0.06) \times 10^{-5} \text{ K}^{-1}$  and  $\phi_a = 1.1 (\pm 0.06) \times 10^{-5} \text{ K}^{-1}$ . The variation of pyromorphite structure can be reflected by the O(1)–Pb(1)–O(2) twist angle ( $\phi$ ) projected on (0001) of the  $\text{Pb(1)O}_6$  metaprism. A quantitative expression was put forward to calculate this angle, which decreases in a linear manner with increasing temperature. It shows that, with the increasing temperature, the  $\text{Pb(1)O}_6$  metaprism undergoes a transformation to trigonal prism, which leads to the increasing of the Pb(1)–O bond length and a volume expansion. A distinct drop of the twist angle was observed at ~1100–1200 K, which could be a sign of the structural collapse and a phase transition to a low symmetric subgroup. A more accurate structural refinement with high X-ray energy and a wider range of data collection or a neutron diffraction experiment will be beneficial to reveal more structural details under different conditions. Yet, the expression and methods we proposed here can be useful to monitor the structural evolution of other apatite group materials.

**Supplementary Materials:** The following are available online at <http://www.mdpi.com/2073-4352/10/12/1070/s1>, cif format files for the refined atom coordinates at each temperature.

**Author Contributions:** Conceptualization, S.Q. and T.G.; methodology, S.Q. and T.G.; software, X.W. and T.G.; formal analysis, T.G. and X.W.; investigation, T.G.; resources, S.Q.; data curation, T.G.; writing—original draft preparation, T.G.; writing—review and editing, S.Q. and X.W.; visualization, T.G.; supervision, S.Q.; funding acquisition, S.Q. All authors have read and agreed to the published version of the manuscript.

**Funding:** This research was funded by National Science Foundation of China, grant number 41772034, dedicated to Qin.

**Acknowledgments:** We would like to thank Hejin Wang for his technical support for XRD data collection. Part of this work was initially presented at International School of Crystallography, 44th course: The Power of Powder Diffraction, Erice, Italy, and T.G. would like to thank the financial support during the conference from the meeting committee.

**Conflicts of Interest:** The authors declare no conflict of interest.

## References

1. McConnell, D. *Apatite: Its Crystal Chemistry, Mineralogy, Utilization, and Geologic and Biologic Occurrences*; Applied Mineralogy; Springer: Wien, Austria, 1973; pp. 22–32.
2. White, T.J.; Dong, Z.L. Structural derivation and crystal chemistry of apatites. *Acta Crystallogr. B Struct. Sci.* **2003**, *59*, 1–16. [[CrossRef](#)] [[PubMed](#)]
3. Schriewer, M.S.; Jeitschko, W. Preparation and crystal structure of the isotypic orthorhombic strontium perrhenate halides  $\text{Sr}_5(\text{ReO}_5)_3\text{X}$  ( $\text{X} = \text{Cl}, \text{Br}, \text{I}$ ) and structure refinement of the related hexagonal apatite-like compound  $\text{Ba}_5(\text{ReO}_5)_3\text{Cl}$ . *J. Solid State Chem.* **1993**, *107*, 1–11. [[CrossRef](#)]
4. Shearer, C.K.; Burger, P.V.; Papike, J.J.; McCubbin, F.M.; Bell, A.S. Crystal chemistry of merrillite from Martian meteorites: Mineralogical recorders of magmatic processes and planetary differentiation. *Meteorit. Planet. Sci.* **2015**, *50*, 649–673. [[CrossRef](#)]
5. Yaroshevsky, A.A. Abundances of chemical elements in the Earth's crust. *Geochem. Int.* **2006**, *44*, 48–55. [[CrossRef](#)]
6. Boyce, J.W.; Liu, Y.; Rossman, G.R.; Guan, Y.; Eiler, J.M.; Stolper, E.M.; Taylor, L.A. Lunar apatite with terrestrial volatile abundances. *Nature* **2010**, *466*, 466–469. [[CrossRef](#)] [[PubMed](#)]
7. Chen, X.; Wright, J.V.; Conca, J.L.; Peurrung, L.M. Evaluation of heavy metal remediation using mineral apatite. *Water Air Soil Pollut.* **1997**, *98*, 57–78. [[CrossRef](#)]
8. Kim, J.Y.; Dong, Z.; White, T. Model apatite systems for the stabilization of toxic metals: II, cation and metalloid substitutions in chlorapatites. *J. Am. Ceramic Soc.* **2005**, *88*, 1253–1260. [[CrossRef](#)]
9. Ibrahim, M.; Labaki, M.; Giraudon, J.-M.; Lamonier, J.-F. Hydroxyapatite, a multifunctional material for air, water and soil pollution control—A review. *J. Hazard. Mater.* **2019**, *383*, 121139. [[CrossRef](#)] [[PubMed](#)]
10. Hovis, G.L.; Scott, B.T.; Altomare, C.M.; Leaman, A.R.; Morris, M.D.; Tomaino, G.P.; McCubbin, F.M. Thermal expansion of fluorapatite-hydroxylapatite crystalline solutions. *Am. Mineral.* **2014**, *99*, 2171–2175. [[CrossRef](#)]
11. Hovis, G.; Abraham, T.; Hudacek, W.; Wildermuth, S.; Scott, B.; Altomare, C.; Medford, A.; Conlon, M.; Morris, M.; Leaman, A.; et al. Thermal expansion of F-Cl apatite crystalline solutions. *Am. Mineral.* **2015**, *100*, 1040–1046. [[CrossRef](#)]
12. Chernorukov, N.G.; Knyazev, A.V.; Bulanov, E.N. Phase transitions and thermal expansion of apatite-structured compounds. *Inorg. Mater.* **2011**, *47*, 172–177. [[CrossRef](#)]
13. Knyazev, A.V.; Chernorukov, N.G.; Bulanov, E.N. Phase diagram of apatite system  $\text{Ca}_{10}(\text{PO}_4)_6\text{Cl}_2\text{-Pb}_{10}(\text{PO}_4)_6\text{Cl}_2$ . *Thermochim. Acta* **2011**, *526*, 72–77. [[CrossRef](#)]
14. Tzvetanova, Y. Lead phosphate minerals from Brussevtzi deposit (Eastern Rhodopes, Bulgaria)-SEM, JR and DTA studies. *Comptes Rendus Acad. Bulg. Sci.* **2003**, *56*, 5–55.
15. McCusker, L.B.; von Dreele, R.B.; Cox, D.E.; Louër, D.; Scardi, P. Rietveld refinement guidelines. *J. Appl Crystallogr.* **1999**, *32*, 36–50. [[CrossRef](#)]
16. Dai, Y.; Hughes, J. Crystal structure refinements of vanadinite and pyromorphite. *Can. Mineral.* **1989**, *27*, 189–192.
17. Lytle, D.A.; Schock, M.R. The formation of Pb(IV) oxides in chlorinated water. *J. Am. Water Works Assoc.* **2005**, *97*, 102–114. [[CrossRef](#)]
18. Bauer, M.; Klee, W.E. The monoclinic-hexagonal phase transition in chlorapatite. *Eur. J. Mineral.* **1993**, *5*, 307–316. [[CrossRef](#)]
19. Shannon, R. Revised effective ionic radii and systematic studies of interatomic distances in halides and chalcogenides. *Acta Crystallogr. Sect. A Cryst. Phys. Diffr. Theor. Gen. Crystallogr.* **1976**, *32*, 751–767. [[CrossRef](#)]

**Publisher's Note:** MDPI stays neutral with regard to jurisdictional claims in published maps and institutional affiliations.



© 2020 by the authors. Licensee MDPI, Basel, Switzerland. This article is an open access article distributed under the terms and conditions of the Creative Commons Attribution (CC BY) license (<http://creativecommons.org/licenses/by/4.0/>).